Monthly Notices of the ROYAL ASTRONOMICAL SOCIETY

MNRAS 532, 4261–4271 (2024)
Advance Access publication 2024 July 19

https://doi.org/10.1093/mnras/stae1760

The thermodynamic response of heating at coronal null points

D. Johnson ,[1★] A. W. Hood,[1] P. J. Cargill,[1,2] J. Reid[1] and C. D. Johnston[3,4]

[1] *School of Mathematics and Statistics, University of St Andrews, St Andrews, Fife KY16 9SS, UK*
[2] *The Blackett Laboratory, Imperial College, London SW7 2BW, UK*
[3] *Department of Physics and Astronomy, George Mason University, Fairfax, VA 22030, USA*
[4] *NASA Goddard Space Flight Center, Greenbelt, MD 20771, USA*

Accepted 2024 July 15. Received 2024 July 11; in original form 2024 May 3

ABSTRACT

Magnetic null points are an important aspect of the magnetic field structure of the solar corona and can be sites of enhanced dissipation. This paper uses analytical and numerical models to investigate the plasma structure around a heated null. It is shown that the temperature profile not only differs significantly from that in a uniform field, but also that the profile depends significantly on the spatial structure of the heating. Field lines close to the separatrices and the null point have higher temperatures than a uniform field for the same heating input. The dependence of the results near the null on both the ratio of perpendicular to parallel conduction, and numerical resolution is also explored. The comparison between analytic and numerical solutions also provides a useful benchmark to compare MHD codes with anisotropic thermal conduction.

Key words: conduction – Sun: corona – Sun: magnetic fields.

1 INTRODUCTION

The heating of the solar corona is a highly topical research area and several possible heating mechanisms have been suggested (e.g. Heyvaerts & Priest 1983; Klimchuk 2006; Van Doorsselaere, Andries & Poedts 2007; Hood, Browning & Van der Linden 2009; Parnell & De Moortel 2012; De Moortel & Browning 2015). One is the dissipation of hydromagnetic waves which we discuss in Section 5. An alternative (e.g. Parker 1972; Cargill, Warren & Bradshaw 2015) is that magnetic energy is slowly stored in the coronal magnetic field and released in a series of small reconnection events, often termed ‘nanoflares’ (e.g. Parker 1988). This is commonly discussed in terms of field line braiding (e.g. Zirker & Cleveland 1993; Pontin et al. 2016), where the local magnetic field becomes mis-aligned, permitting reconnection, which in turn leads to heating and particle acceleration in the vicinity of the reconnection site. In terms of the plasma properties, for quasi-steady heating, an equilibrium is attained among the heating, thermal conduction and optically thin radiation (e.g. Rosner, Tucker & Vaiana 1978), though footpoint heating can lead to different outcomes (e.g. Antiochos & Klimchuk 1991; Froment et al. 2018). For impulsive heating, defined as arising when the duration of the heating is shorter than the characteristic timescale of plasma cooling, the plasma first cools by conduction, then by radiation (e.g. Cargill, Mariska & Antiochos 1995). The conductive cooling time scales as $T^{-5/2}$ and, for typical active region parameters, it is of order a few hundred seconds, shorter than cooling due to optically thin radiation at such temperatures. However, if very high temperatures, of order 10 MK, are reached, as suggested by some observations (e.g. Reale et al. 2009; Testa & Reale 2012; Parenti et al. 2017), the cooling of hot plasma is very rapid in such braided fields, and this poses major challenges for detectability (e.g. Barnes, Cargill & Bradshaw 2016).

There is though another coronal magnetic configuration associated with dissipation, namely a magnetic null point (e.g. Lau & Finn 1990; Parnell et al. 1996; Brown & Priest 2001). Their copious existence are inferred by Close, Parnell & Priest (2004), Régnier, Parnell & Haynes (2008), and Longcope & Parnell (2009) and observed by Cheng et al. (2023). Such null points are domains of weak magnetic field and it has been suggested (e.g. Galsgaard & Pontin 2011) that stressing the magnetic field near these points will result in the build-up of strong currents there, which then dissipate through direct plasma heating and (viscously damped) mass motions. Thus, heating associated with the null is not a local process, with a significant plasma volume being heated. While the build up and dissipation of magnetic energy at such nulls has been widely investigated (e.g. Craig & McClymont 1991; McLaughlin & Hood 2004, 2006; McLaughlin 2013), the thermodynamic response of the plasma to heating events, and to associated energy transport, in the neighbourhood of coronal null points has not been studied in any detail. That is the aim of this and subsequent papers.

In the strong field limit thermal conduction is aligned with the magnetic field (Braginskii 1965). However, the null introduces some potentially significant differences to conductive transport. Firstly, as the field around the null becomes small, thermal conduction must reduce to the isotropic form, while a full anisotropic conduction must be implemented elsewhere. Despite many magnetohydrodynamic (MHD) codes having implemented such an anisotropic heat conduction, there has been no quantification of how they cope with null points. Secondly, the magnetic field strength around the null is highly non-uniform. It is well known that the cross-section of a magnetic flux element has a significant influence on conductive

★ E-mail: dj57@st-andrews.ac.uk

cooling, with strongly diverging field lines leading to inhibition (e.g. Antiochos & Sturrock 1976; Cargill et al. 2022). This may have observational consequences at nulls.

This paper presents an investigation of the plasma response to null point heating in the neighbourhood of a 2D, X-type null point. We present analytic solutions of the temperature distribution near a null for various steady-state heating scenarios, and compare these with numerical solutions of the MHD equations. Of particular importance is the investigation of the dependence of the solutions on the parametrization of the anisotropic conductivity and the numerical resolution. In one case, the temperature is *always* unresolved in some locations. Thus, these analytic solutions provide a stringent test for any MHD code that purports to model anisotropic conduction. The basic equations used are presented in Section 2, a brief description of thermal conduction near a null point given in Section 3, with a more detailed description of the thermal conductivity given in Appendix A. The results for two forms of heating function are resented in Section 4 and the conclusions are presented in Section 5.

2 MHD EQUATIONS AND NUMERICAL METHOD

The thermodynamic evolution of a coronal plasma near a 2D magnetic null point is studied using both analytical and numerical methods. The latter involves solving the time-dependent MHD equations which take the following form:

$$\frac{\partial \rho}{\partial t} + \nabla \cdot (\rho \mathbf{v}) = 0\,, \tag{1}$$

$$\rho\frac{\partial \mathbf{v}}{\partial t} + \rho \mathbf{v}\cdot\nabla\mathbf{v} = -\nabla p + \mathbf{j}\times\mathbf{B} + \mathbf{F}_{shock}, \tag{2}$$

$$\frac{\partial \mathbf{B}}{\partial t} = \nabla\times(\mathbf{v}\times\mathbf{B}) - \nabla\times(\eta\nabla\times\mathbf{B}), \tag{3}$$

$$\rho\left(\frac{\partial \varepsilon}{\partial t} + \mathbf{v}\cdot\nabla\varepsilon\right) = -p\nabla\cdot\mathbf{v} + \nabla\cdot(\boldsymbol{\kappa}\cdot\nabla T) + H, \tag{4}$$

$$p = 2\rho\tfrac{k_B}{m}T\,. \tag{5}$$

The equations are solved using the Lagrangian–Remap scheme, *Lare* (Arber et al. 2001) and appropriate boundary and initial conditions are imposed, as discussed later. The variables: ρ, $\mathbf{v}$, p, $\mathbf{B}$ and $\varepsilon = p/(\rho(\gamma-1))$ are the mass density, velocity, gas pressure, associated magnetic field and specific internal energy respectively. The current density is defined as $\mathbf{j} = \nabla\times\mathbf{B}/\mu_0$. The *Lare* code (Arber et al. 2001) is a shock capturing second-order accurate finite volume code that uses a staggered grid. During one timestep, it first updates the MHD equations on a Lagrangian grid, that moves with the flow, before remapping back to the fixed Eulerian one. The magnetic field is time advanced using the constrained transport method (Evans & Hawley 1988), ensuring that $\nabla\cdot\mathbf{B} = 0$ for all time if it is zero initially. *Lare* imposes shock viscosities, $\mathbf{F}_{shock}$, which are influential in regions of strong gradients in velocities. These are discussed in Arber et al. (2001), Van Leer (1997), Caramana, Shashkov & Whalen (1998) and Reid et al. (2020, appendix A1). The plasma parameters are the ratio of specific heats, $\gamma = 5/3$, the magnetic diffusivity, $\eta = 1/(\mu_0\sigma)\,(\mathrm{m^2s^{-1}})$ and the electrical conductivity, σ (Ωm). The permeability of free space is $\mu_0 = 4\pi\times10^{-7}\,\mathrm{Hm^{-1}}$. The anisotropic thermal conductivity tensor $\boldsymbol{\kappa}$ is discussed later. All heating terms, including shock, viscous, and Ohmic (j^2/σ) heating are incorporated into H. Optically thin radiative losses are not modelled in this work, as they are found to make no appreciable difference to the findings presented in this paper (see also Section 4).

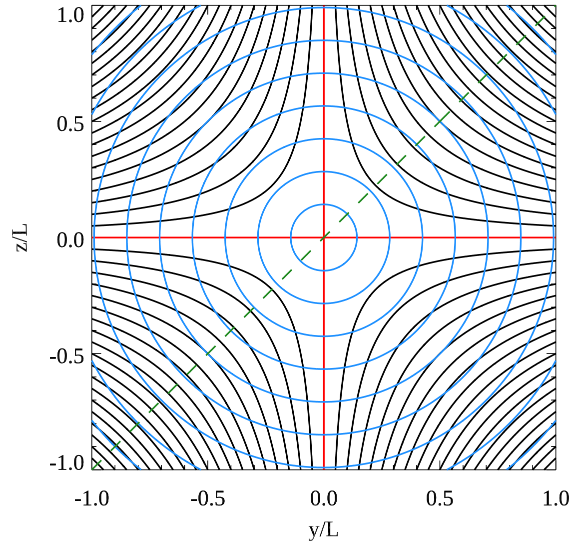

Figure 1. The magnetic field structure including separatrices (red curves along y = 0 and z = 0) and contours of constant field magnitude (blue concentric circles) about a null point. The diagonal (green) dashed line indicates where $y = z$.

The equations solved by *Lare*3D are made dimensionless in the usual way (e.g. Botha et al. 2000; Gerrard et al. 2001, 2003) with a reference density of $\rho_0 = 1.67\times10^{-12}\mathrm{kg/m^3}$, magnetic field strength of $B_0 = 10^{-2}$ T (100 G) and length of $L = 5\times10^7$m. A dimensionless uniform background diffusivity of $\eta = \eta_b = 10^{-5}$ is imposed, which corresponds to a physical value of $\eta = 3.45\times10^9 m^2 s^{-1}$.

This work aims to understand the thermodynamic response of a coronal plasma to heating at a null point therefore we impose the spatial form of H artificially. Self-consistent heating requires heating sources that may introduce unwanted additional complexities, such as reconnection at the null (e.g. Craig & McClymont 1991) or wave motion near the null (e.g. McLaughlin & Hood 2004; Prokopyszyn, Hood & De Moortel 2019). Further discussion of the nature of heating near a null is presented in Section 5. Although our imposed heating may be simplistic, it yields tractable analytical equilibrium solutions that are compared with numerical solutions. All plots show temperature in Kelvin, but normalized values for lengths, unless otherwise stated. All derivations and discussion uses normalized quantities, unless otherwise stated.

3 THERMAL CONDUCTION IN A MAGNETIC FIELD WITH A NULL POINT

We consider a magnetic field with a simple 2D null point in Cartesian coordinates of the form

$$\mathbf{B} = \frac{B_0}{L}(0, y, -z)\,, \tag{6}$$

where B_0 and L are defined above. Fig. 1 shows the field lines and contours of constant field magnitude, where the field strength increases linearly with radial distance from the origin.

When investigating cooling via thermal conduction, it is convenient to assume thermal conduction is only field-aligned (e.g. Antiochos & Sturrock 1976; Cargill et al. 2022). However, perpendicular thermal conductivity becomes increasingly important as the magnetic field strength weakens and heat flux becomes isotropic at a null, where the field vanishes. Appendix A presents a more detailed discussion of the general expression for thermal conductivity in a magnetic field, but here we note that thermal conduction is given by

$$\nabla \cdot (\boldsymbol{\kappa} \cdot \nabla T) = \nabla \cdot \left(\kappa_\parallel \frac{\mathbf{B} \cdot \nabla T}{B^2} \mathbf{B} \right) + \nabla \cdot \left(\kappa_\perp \left(\nabla T - \frac{\mathbf{B} \cdot \nabla T}{B^2} \mathbf{B} \right) \right), \quad (7)$$

where the perpendicular conductivity, $\kappa_\perp$, is approximated by

$$\kappa_\perp \approx \frac{\kappa_\parallel}{1 + \Omega_e^2 \tau^2}. \quad (8)$$

The electron gyrofrequency is $\Omega_e = eB/m_e$ and the electron-electron collision time, τ, is given (as defined in Woods 1987) by

$$\tau = \left(\frac{\sqrt{4\pi\varepsilon_0}}{e} \right)^4 \frac{3\sqrt{m_e}(k_B T)^{3/2}}{4\sqrt{2\pi} n \lambda}, \quad (9)$$

where e is the elementary charge, B the magnetic field strength, k_B Boltzmann's constant, T the temperature, n the electron number density, ε_0 the permittivity of free space and λ the Coulomb logarithm, assumed to be 20. In the strong field limit, $\Omega_e \tau \gg 1$ and $\kappa_\perp \approx \kappa_\parallel/(\Omega_e \tau)^2$, such that perpendicular conductivity is frequently neglected. In order to quantify where perpendicular thermal conduction becomes important, we define this to arise when $(\Omega_e \tau)^2 < 1$ which occurs when the magnetic field strength, $B = |\mathbf{B}|$, falls below a value $B_{\min}^2 = m_e^2/e^2\tau^2$. Note that $B_{\min}$ as defined here should not be confused with the minimum of the field strength but is the value of the field strength at which $(\Omega_e \tau)^2 = 1$. As we note below, for the simple null field, this condition translates into a simple expression for the distance away from the null where perpendicular conduction becomes important. Although $B_{\min}^2 \propto n^2/T^3$, we ignore this dependence and assume here that it is just a spatio-temporal constant, determined by characteristic temperatures, densities and various fundamental constants. However, we note that $B_{\min}^2$ does become smaller with increasing temperature, at constant pressure. More details are given in Braginskii (1965), Balescu (1988a, b), Boyd & Sanderson (2003) and Appendix A. Thus, from equation (7), the thermal conduction term is described by

$$\nabla \cdot (\boldsymbol{\kappa} \cdot \nabla T) = \nabla \cdot \left(\frac{\kappa_\parallel (\mathbf{B} \cdot \nabla T)\mathbf{B}}{B_{\min}^2 + B^2} \right) + \nabla \cdot \left(\frac{B_{\min}^2 \kappa_\parallel}{B_{\min}^2 + B^2} \nabla T \right). \quad (10)$$

This reduces to field-aligned thermal conduction (the form used in equation (16) below), in the usual strong field limit, $B^2 \gg B_{\min}^2$. However, if $B = 0$, thermal conduction is isotropic. Substituting $\kappa_\parallel = \kappa_0 T^{5/2}$, with $\kappa_0 = 10^{-11}$ W K$^{-7/2}$ m^{-1}, the magnetic field given by equation (6) and defining

$$G = \frac{2\kappa_0 T^{7/2}}{7L^2}, \quad (11)$$

thermal conduction can be written in terms of the differential operator, $\mathcal{F}$,

$$\begin{aligned} \mathcal{F}(G) = & \frac{\partial}{\partial y} \left[\frac{y^2 + B_{\min}^2}{B_{\min}^2 + r^2} \frac{\partial G}{\partial y} \right] - \frac{\partial}{\partial y} \left[\frac{yz}{B_{\min}^2 + r^2} \frac{\partial G}{\partial z} \right] \\ & - \frac{\partial}{\partial z} \left[\frac{zy}{B_{\min}^2 + r^2} \frac{\partial G}{\partial y} \right] + \frac{\partial}{\partial z} \left[\frac{z^2 + B_{\min}^2}{B_{\min}^2 + r^2} \frac{\partial G}{\partial z} \right], \end{aligned} \quad (12)$$

where $r^2 = y^2 + z^2$. Note that equation (12) reduces to

$$\mathcal{F}(G) = \frac{\partial^2 G}{\partial y^2} + \frac{\partial^2 G}{\partial z^2}, \quad (13)$$

when $B_0^2 r^2/L^2 \ll B_{\min}^2$. In the opposite limit, $B_0^2 r^2/L^2 \gg B_{\min}^2$, it reduces to the usual anisotropic form for parallel heat conduction. The strong field limit breaks down as $\Omega_e^2 \tau^2 \to 1$ which, in practice, should motivate the value of $B_{\min}^2$. equation (9) shows that for typical coronal conditions ($T = 10^6$ K and $n = 10^{15}$ m^{-3}) $\Omega_e^2 \tau^2 = 1$ when $|B| = 4.13 \times 10^{-10}$ T, which corresponds to a radius of 2.06 m in the null point field, stated above. Table 1 shows how this threshold magnetic field strength, $|B|$ (upper section), and the equivalent radius (for the model null point in this work; lower section) vary with temperature and density. Clearly, there is a very small region surrounding a coronal null point, of order several meters, where thermal conduction perpendicular to the magnetic field is important. However, Table 1 shows that this range rapidly increases by several orders of magnitude as the plasma becomes cool and dense. Although this region around the null point is small, it influences the temperature all along the separatrices.

Table 1. This table (top half) illustrates how $|B|$ satisfying $\Omega_e^2 \tau^2 = 1$ varies depending on temperature and the product of density and the Coulomb logarithm and (bottom half) shows the radii where each $|B|$ (above) is in the model used in this work.

	$\lambda n = 10^{20}$ m^{-3}	$\lambda n = 10^{18}$ m^{-3}	$\lambda n = 10^{16}$ m^{-3}
T = 10^4 K	2.07×10^{-3} T	2.07×10^{-5} T	2.07×10^{-7} T
T = 10^5 K	6.54×10^{-5} T	6.54×10^{-7} T	6.54×10^{-9} T
T = 10^6 K	2.07×10^{-6} T	2.07×10^{-8} T	2.07×10^{-10} T
T = 10^7 K	6.54×10^{-8} T	6.54×10^{-10} T	6.54×10^{-12} T
T = 10^4 K	1.04×10^7 m	1.04×10^5 m	1.04×10^3 m
T = 10^5 K	3.27×10^5 m	3.27×10^3 m	3.27×10^1 m
T = 10^6 K	1.04×10^4 m	1.04×10^2 m	1.04×10^0 m
T = 10^7 K	3.27×10^2 m	3.27×10^0 m	3.27×10^{-2} m

4 THERMAL EQUILIBRIUM NEAR A NULL POINT

We assume that any thermal equilibrium is a balance between an imposed heating function and anisotropic thermal conduction. This implies the neglect of optically thin radiation. The ratio of conductive to radiative losses is approximately $5 \times 10^{20} T^4/(nL)^2$, where a loss function $\Lambda(T) \propto T^{-1/2}$ is used (e.g. Rosner et al. 1978; Cargill 1993). For $n = 10^{15}$ m^3, $T = 3 \times 10^6$ K and $L = 25$ Mm, this ratio is 60 so that conductive losses will tend to dominate and such dominance increases as T increases. We have run a limited number of simulations including optically thin radiative losses and see no quantitative difference in the results.

In the following, three approaches are used to derive the thermal equilibrium near a null point, namely an analytical solution and two numerical methods. This allows us to assess the accuracy of the two numerical schemes. While the number of grid points used in the numerical models is varied to study the effect of different resolutions, results are shown for a grid of 1024 × 1024 cells unless stated otherwise. Similarly, $B_{\min}^2 = 10^{-10}$, unless otherwise stated. This is small enough to allow a meaningful comparison with the analytical solution, which implicitly assumes $B_{\min}^2 = 0$, but large enough to ensure there are no divisions by zero at the null in the numerical cases.

4.1 Equations

In the analytical approach, we solve

$$\mathcal{F}(G) = -H(y, z), \quad (14)$$

directly for two different forms of coronal heating, as discussed below. This provides a useful test for checking the accuracy of two distinct numerical methods. In the first numerical approach, the 2D MHD equations given in equations (1)–(5) are solved, using the MHD code *Lare* (Arber et al. 2001), to follow the plasma as it relaxes to a thermal equilibrium. Thermal conduction is included and particular forms of coronal heating, H, are used, as discussed below. Also present are the usual shock viscosities and resistivity, and consequently shock and Ohmic heating. However, as the plasma tends towards an equilibrium, the velocities tend to zero and, consequently, there is no shock heating once equilibrium is reached. Similarly, since the initial magnetic field is potential and is fixed at the domain boundaries, strong currents tend not to form, such that Ohmic heating is minimal. Thus, the final thermal equilibrium is determined by the imposed heating, H. In practice, we find that the imposed heating accounts for approximately 99.9 per cent of the total heating.

There are some important subtleties in this numerical approach that need to be considered in any code benchmarking. The staggered grid means that temperature and density are evaluated at the centres of cells, the velocity on the corners of cells and each magnetic field component on a different cell face (see Arber et al. 2001, fig. 1). This set up means that the null point in our problem should be located on a cell corner therefore the temperature and magnetic field are not defined at the theoretical location of the null. Any simple interpolation scheme used to estimate the null point temperature will require some averaging, introducing numerical diffusion. Other codes will introduce various levels of diffusion and additional discrepancies depending on whether (i) all magnetic field components are co-spatial or not; (ii) the grid is adaptive (so that the null may be temporarily on a grid point); or (iii) the temperature is defined at the null. Obviously, all of these effects are reduced as the grid resolution is improved and, theoretically, all codes should produce the same results. Practically, one must use a sufficiently fine resolution such that these issues are small. We discuss this further in Section 4.4, where the influence of grid resolution is presented.

In the second numerical approach, we use a relaxation code that solves

$$\frac{\partial G}{\partial t} = \mathcal{F}(G) + H, \tag{15}$$

where G is defined above and only requires the temperature to be stored. Additionally, we impose $B_{\min}^2 = 0$ for this numerical solution. In this approach, the temperature is evaluated at the cell corners, hence at the null point. However, the same finite differencing, as *Lare*, is used so that both are second-order accurate. The relaxation scheme only evolves the temperature, but it will relax to the same equilibrium temperature as *Lare*. As there is no averaging needed to determine the null point temperature, we can immediately see the effect of grid resolution without any additional numerical diffusion.

Finally, because the time evolution is not relevant and only the equilibrium temperature is important, convergence towards the final equilibrium can be accelerated using Aitken's delta squared method (Aitken 1927) on a sequence of time dumps. This process is also applied to the *Lare* solution to verify that it has fully relaxed. Hence, we can verify the accuracy of the *Lare* results by comparing with our analytical solution and with our relaxation method.

4.2 Boundary conditions

For the analytical and second numerical solutions, we impose $T = T_b$ ($T_b = 2 \times 10^4$ K) at $y = \pm 1$ and $z = \pm 1$. *Lare* defines the temperature at cell centres therefore the *Lare* solutions fix the temperature in the boundaries, at $y = \pm 1 \pm h/2$ and $z = \pm 1 \pm h/2$ (where h is the width of each grid cell). The magnetic field components and the density have zero normal derivatives and so the density (and thus pressure) can adjust at the boundaries. The final equilibrium, after the relaxation stage, will have pressure constant along field lines but not necessarily constant across the field. Note that the pressure variation does not influence the temperature equilibrium, when radiation is neglected, and has a minimal change to the magnetic field. Finally, all velocity components are zero on all boundaries so that the total mass in the simulation box is conserved.

4.3 Heating constant in time

We consider the equilibrium temperature structure when the imposed coronal heating function is constant in time and is either taken as spatially uniform (Section 4.3.1) or proportional to B^2 (Section 4.3.2). The latter can be argued to be a proxy for Ohmic heating and gives more heating near the boundaries.

4.3.1 Constant uniform heating

For spatially and temporally constant heating, an analytical solution can be obtained away from the null point: thus, we set $B_{\min}^2 = 0$ for this section. Note that the *Lare* models retain $B_{\min}$.

For constant heating, the energy balance is between conduction and heating,

$$\mathbf{B} \cdot \nabla \left(\frac{\kappa_0 T^{5/2}}{B^2} \mathbf{B} \cdot \nabla T \right) = -H. \tag{16}$$

It is convenient to renormalize the equation and non-dimensionalize G as

$$\bar{G} = \frac{G}{H}, \tag{17}$$

where G is given by equation (11) and H is a constant. Then, equation (16) becomes

$$\left(y\frac{\partial}{\partial y} - z\frac{\partial}{\partial z} \right) \left(\frac{y}{y^2+z^2}\frac{\partial \bar{G}}{\partial y} - \frac{z}{y^2+z^2}\frac{\partial \bar{G}}{\partial z} \right) = -1\,. \tag{18}$$

Solving this for $\bar{G} = C + F(y, z)$, with $F = 0$ on all the boundaries and where C is a constant, defines the function $F(y, z)$, and the temperature for general heating is given by

$$T = T_b \left(1 + \frac{7}{2}\frac{HL^2}{\kappa_0} F(y, z) \right)^{2/7}. \tag{19}$$

The important point is that the function $F(y, z)$ is independent of the value of the heating. We define new coordinates based on the flux function, A, and another orthogonal coordinate related to the distance along a field line (e.g Bulanov & Syrovatskii 1980; McLaughlin, Hood & De Moortel 2011):

$$A = yz \text{ and } \xi = \frac{1}{2}\left(y^2 - z^2\right)\,, \tag{20}$$

or equivalently

$$y^2 = \sqrt{A^2+\xi^2} + \xi \text{ and } z^2 = \sqrt{A^2+\xi^2} - \xi. \tag{21}$$

Note, for reference, that the distance along a field line, s, is defined by

$$\frac{\mathrm{d}y}{\mathrm{d}s} = \frac{y}{\sqrt{y^2+z^2}} \quad \text{and} \quad \frac{\mathrm{d}z}{\mathrm{d}s} = -\frac{z}{\sqrt{y^2+z^2}}\,. \tag{22}$$

Hence, using the coordinates ξ and A,

$$\frac{y}{y^2+z^2}\frac{\partial \bar{G}}{\partial y} - \frac{z}{y^2+z^2}\frac{\partial \bar{G}}{\partial z} = \frac{\partial \bar{G}}{\partial \xi}\,. \tag{23}$$

Now, equation (18) can be written as

$$\left(y^2+z^2\right)\frac{\partial^2 \bar{G}}{\partial \xi^2} = 2\sqrt{A^2+\xi^2}\frac{\partial^2 \bar{G}}{\partial \xi^2} = -1. \tag{24}$$

This can be solved to get

$$\bar{G} = D(A) + C(A)\xi + \frac{1}{2}\sqrt{A^2+\xi^2} - \frac{\xi}{2}\sinh^{-1}\left(\frac{\xi}{A}\right), \tag{25}$$

where, again, C and D are functions of A. If $\bar{G}$ is symmetric about $\xi = 0$, then $C(A) = 0$. There are other forms for this solution. For example, we can use

$$\sinh^{-1}\left(\frac{\xi}{A}\right) = \mathrm{sgn}(A)\left(\ln\left[\xi + \sqrt{A^2+\xi^2}\right] - \ln|A|\right), \tag{26}$$

where the sign function, sgn(A), is defined as

$$\mathrm{sgn(A)} = \begin{cases} 1\,, & A > 0\,, \\ 0\,, & A = 0\,, \\ -1\,, & A < 0\,. \end{cases}$$

This demonstrates that there is a logarithmic singularity as $A \to 0$ and this general solution is not valid at $A = 0$. If we choose $\bar{G} = \bar{G}_b = \frac{2}{7}\frac{\kappa_0}{L^2 H}T_b^{7/2}$ at $z = \pm 1$ for all y and at $y = \pm 1$ for all z, then

$$D(A) = \bar{G}_b - \frac{1}{4}(A^2+1) + \frac{1}{4}(A^2-1)\sinh^{-1}\left(\frac{A^2-1}{2|A|}\right). \tag{27}$$

Hence,

$$\begin{aligned}\bar{G} = \bar{G}_b &- \frac{1}{4}\left(y^2z^2+1\right) + \frac{1}{4}\left(y^2z^2-1\right)\sinh^{-1}\left(\frac{y^2z^2-1}{2|yz|}\right) \\ &+ \frac{1}{4}\left(y^2+z^2\right) - \frac{1}{4}\left(y^2-z^2\right)\sinh^{-1}\left(\frac{y^2-z^2}{2|yz|}\right).\end{aligned} \tag{28}$$

Finally, using equation (26), this can be expressed as

$$\begin{aligned}\bar{G} = \bar{G}_b &- \frac{1}{4}\left(1-y^2\right)\left(1-z^2\right) - \frac{1}{4}\left(1+y^2\right)\left(1-z^2\right)\ln|y| \\ &- \frac{1}{4}\left(1+z^2\right)\left(1-y^2\right)\ln|z|\,.\end{aligned} \tag{29}$$

Specifying $\bar{G}_b$ determines the solution at all locations. Note that in the limit of $y \to 0$ and $z \to 0$ the solution does not exist. However, because we expect $B^2_{\rm min}$ to be small, this solution will give a good description of the temperature everywhere except at the null *and* on the seperatrices. The logarithmic singularity along the seperatrices will be removed by the inclusion of a non-zero value for $B^2_{\rm min}$.

Solving the MHD equations numerically using *Lare*, and in the absence of optically thin radiation, the plasma is simply allowed to relax from an isothermal initial state towards the final equilibrium state. Here we choose a value of the heating that gives a coronal temperature of approximately 2 MK, by selecting $\bar{G}_b$

$$\bar{G}_b = \frac{2}{7}\frac{\kappa_0\left(2\times 10^4\right)^{7/2}}{\left(5\times 10^7\right)^2 H} = 1.18\times 10^{-7},$$

where $H = 1.10 \times 10^{-5}\,\mathrm{Jm^{-3}s^{-1}}$. Different values of $\bar{G}_b$ therefore give a simple rescaling of the temperature.

For this case, the temperature equilibrium achieved is shown in the left column (upper panel) of Fig. 2, as a function of y and z. Notice how sharply peaked the temperature is along the seperatrices. In Fig. 2, the left column (lower panel) shows the temperature as a function of y along both the separatrix line, $z = 0$, as a solid black curve, and along $z = 1/2$, as a dashed blue curve. The temperature along the separatrix is smooth but significantly higher than the temperature everywhere else. Note the singular nature of the seperatrices is shown in the lower left figure as the temperature rises sharply as it crosses the separatrix, at $y = 0$, and then falls rapidly back down again on the other side. This is in agreement with the analytical solution presented in Fig. 3. Note that the lower (left) panel requires a little care in interpretation, where $T(y)$ relates to different field lines at different locations, relative to their symmetry point ($y = z$, e.g. Fig. 1). For example, values of $|y|$ close to unity are near the boundary so will be cooler. $y = -0.5$ corresponds to the symmetry location, so is the location of maximum temperature on that particular field line. As $|y|$ decreases, despite moving away from the location of maximum temperature, the field line lengths and the area of a flux element ($\mathcal{A}(s)$) increase, leading to higher temperatures, peaking at the separatrix. The role of the area of a flux element, $\mathcal{A}(s)$, in determining the temperature is discussed shortly.

Next we benchmark our numerical solution using the relaxation methods discussed above, solving the problem for the balance between thermal conduction and heating, both without any dynamical equations and following the dynamical evolution using *Lare*. Thus, the plasma is allowed to relax towards the equilibrium temperature. As $t \to \infty$, the solution relaxes to the equilibrium solution. Although the temporal evolution for the relaxation method is non-physical, the final temperature will be the same as the temperature produced by *Lare* and the analytical solution, to within numerical truncation errors of the two numerical schemes.

Fig. 3 contrasts the temperatures from these approaches in the vicinity of the null. The various curves show relaxation (red, dashed), together with the temperatures from *Lare* (blue, dotted) and the analytic solution (black, solid). In addition, we apply Aitken's method (green, dot–dashed) to the *Lare* results as well. The comparison is now along the diagonal $y = z$ and so shows how the temperature varies *across* field lines at each loop summit. Each value of y corresponds to a field line whose temperature is symmetric about $y = z$, and a maximum at that location. Fig. 1 demonstrates that each value of y maps the associated field line to the boundaries. The three numerical results essentially lie on top of each other and converge with the analytic solution, *except near the null*. The key feature of Fig. 3 is that the analytic solution has a singularity at the null point (because $B^2_{\rm min} = 0$). Both the relaxation and *Lare* solutions smooth this singularity out near the null point, and agree with each other. Hence, because both numerical solutions agree to such a degree, we infer that numerical diffusion must dominate over the effect of $B^2_{\rm min}$ in the *Lare* solution. This is discussed below. However, the analytic solutions are valid where the strong field approximation holds and show an interesting feature near the null, with a region of very high temperatures that the numerical solutions cannot model due to limited resolutions. We return to resolution issues in Section 4.4.

Near the null point, the flux elements associated with the magnetic field have a large cross-sectional area, since $\mathcal{A}(s) \propto 1/B(s)$, but the magnitude of $\mathcal{A}(s)$ decreases rapidly as one moves away from the null. Fig. 4 shows a comparison between the temperature along field lines for the null point magnetic field and for straight field lines of equal length, with the same heating. It shows that, as one samples the longer field lines closer to the null, the null field lines become hotter and the difference between the straight and null point fields grows. Clearly, the area factor of the field near the null inhibits conduction and leads to a hotter temperature than for the straight field.

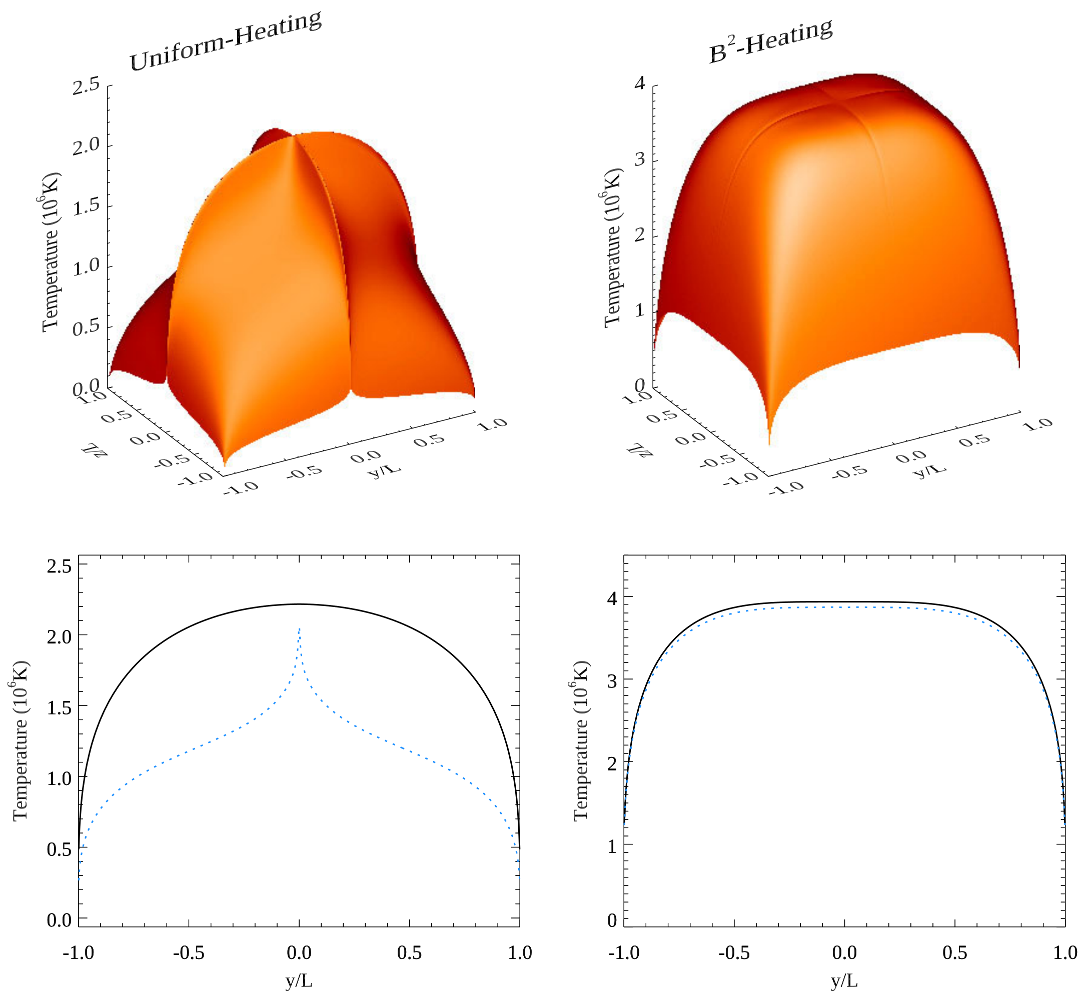

Figure 2. Left column: *Lare* solutions for the temperature, for constant heating, as a function of y and z (top figure) and as a function of y (bottom figure) for $z = 0$ (solid) and $z = 0.5$ (dashed). Note the behaviour as the separatrix is approached at $y = 0$ for the dashed curve. Right column: The corresponding results for heating proportional to B^2.

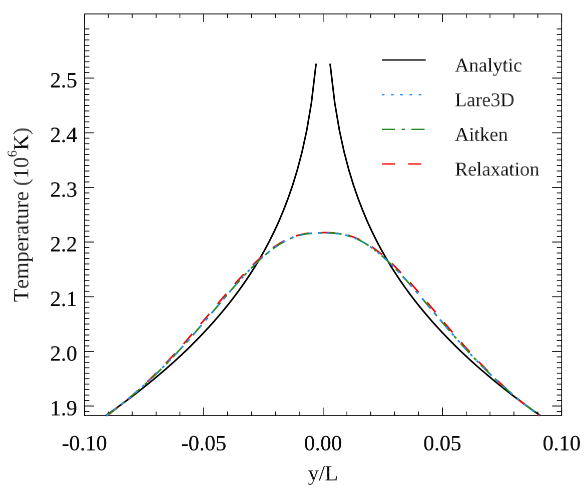

Figure 3. Temperature, for constant heating, as a function of y along $y = z$ near the null for the analytical solution, results from *Lare* and no dynamics relaxation method. The legend in the figure labels each curve.

4.3.2 Heating proportional to B^2

In this case there is more heating at the boundaries of the field lines and corresponds to footpoint heating. Equation (16) becomes

$$\frac{\partial^2 \bar{G}}{\partial \xi^2} = -1 \ . \tag{30}$$

This is equivalent to the equation for a straight uniform magnetic field with constant cross-sectional area but with ξ replaced by a Cartesian coordinate. The solution is given by

$$\bar{G} = D(A) + C(A)\xi - \frac{\xi^2}{2} \ . \tag{31}$$

Thus, $D(A) = \bar{G}_b + (A^2 - 1)^2/8$, $C(A) = 0$ and

$$\bar{G} = \bar{G}_b + \frac{1}{8}\left(1 - y^4\right)\left(1 - z^4\right) \ . \tag{32}$$

Hence, there would be no distinction in temperature between the null and separatrices and the rest of the magnetic field, in contrast to case with uniform heating.

The right column of Fig. 2 presents the numerical relaxation of the temperature for the heating proportional to B^2, as a function of y and z (in the upper panel) and as a function of y (in the lower

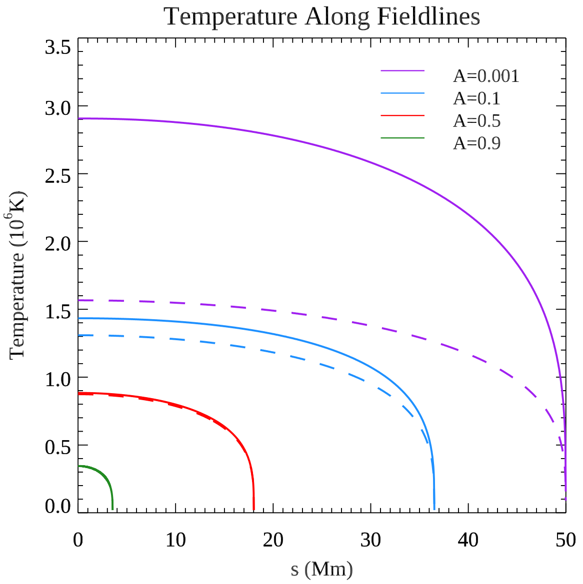

Figure 4. This figure shows a comparison between the equilibrium temperature as a function of the distance, s, along null point field lines (where $s = 0$ is the field line apex) and equivalent length straight field lines, under the same uniform heating. The solid-curves show the analytic null point solution and the dashed curves the straight field solution. The legend specifies the particular field lines, through the value of magnetic vector potential, where $A = yz$.

panel), along $z = 0$ (solid black) and $z = 0.5$ (dashed blue). There is no evidence of any singular temperatures on either the separatrices leading into the null or at the null itself. Both panels of Fig. 2 show that the plasma is almost isothermal around the null, despite there being heating everywhere except at the null.

The difference between this and the previous case can be understood as follows. For uniform heating, the energy deposited at the null cannot be conducted away since the flux elements have infinite cross-sections there. Thus, there is no solution that balances heating and conduction when $\kappa_\perp = 0$. This problem does not arise for the B^2 heating: if there is no heating at the null, an equilibrium becomes possible provided the temperature approaching the null is isothermal, as we find. Thus the 'heating' contributed by the non-uniform area is countered by the diminution of real heating as B approaches zero. However, there must be some heating elsewhere in the corona in order for the conductive flux to be non-zero and match the corona onto a transition region and the cooler chromosphere beneath. Hence, there is a larger conductive flux and the temperature rises more steeply near the boundaries in this case than in the previous uniform heating. (Note that the temperature is now different from the previous case. This is just a consequence of the different heating function.)

The isothermal temperature profile is distinct from what would be expected for a straight magnetic field. The null point field produces higher temperatures than a uniform field, again due to the area variation. We find that along one of the separatrices the null point solution is approximately twice as hot as an equivalent straight field solution, similar to what is shown in Fig. 4 for small A.

4.4 Effect of varying $B^2_{\rm min}$ and numerical resolution

In this section, we consider spatially constant heating and start by varying the magnitude of $B^2_{\rm min}$ (i.e. perpendicular thermal conduction) for 1024 grid points in each direction, and then, for a small fixed value of $B^2_{\rm min} = 10^{-10}$ (which is the default value in *Lare*), vary the number of grid points to assess numerical convergence and the ability of the numerical solutions to capture steep gradients, near the separatrices and the null. Note that heating proportional to B^2 has neither numerical resolution problems nor the need for $B^2_{\rm min}$. Physical models for larger $B^2_{\rm min}$ are discussed later.

Using *Lare*, the upper and middle panels of Fig. 5 show the temperature as a function of y along $y = z$ for six different values of $B^2_{\rm min}$. The upper panel shows the entire domain, the middle panel expands the region around $y = 0$ and the lower panel shows the difference between the numerical solutions for a given $B^2_{\rm min}$ and $B^2_{\rm min} = 10^{-10}$. For $|y| > 0.5$, all the curves lie on top of each other. Although the maximum temperature at $y = 0$ is reduced for larger values of $B^2_{\rm min}$, there is evidence of an increased temperature away from the central peak (lowest plot). Thus compared with the smallest value of $B^2_{\rm min}$ and the analytical solution, the plasma is slightly hotter away from the null point and separatrices (and cooler near them) for larger values of $B^2_{\rm min}$.

Note that curves for $B^2_{\rm min} = 10^{-10}$ and 10^{-8} lie on top of each other (so only $B^2_{\rm min} = 10^{-10}$ is plotted). This indicates that numerical diffusion is more important than perpendicular diffusion at such small values of $B^2_{\rm min}$. Setting $B^2_{\rm min} = 0$, will not change these results and will not increase the null point temperature. However, increasing the number of grid points will reduce numerical diffusion and increase the temperature. As the number of grid points tends to infinity, the numerical diffusion will be reduced and these two curves will vary from each other due to the perpendicular conduction near the null point.

We now fix $B^2_{\rm min} = 10^{-10}$, and vary the resolution, to investigate the implications of convergence and numerical diffusion. Fig. 6 shows the temperature plotted along the diagonal, $y = z$, as a function of y (the green dashed curve in Fig. 1). The left panel shows an expanded view near the null point at $y = 0$. Note the singular nature of the analytic solution (black dashed) at the null point. Obviously, the closest approximation to the analytic solution comes from the finest resolution, with the largest number of grid points ($n = 2048$ - teal curve). As the number of grid points is reduced, numerical diffusion becomes more important and results in a reduction of the temperature at the null point (and on the separatrices) and enhancement elsewhere. The variation in temperature, away from the null, is shown in the right panel, where for $y > 0.2$, the temperature reduces over most of the domain as the number of grid points increases. The figure demonstrates that the numerical solutions are converging as the curves start to lie on top of each other. Note that as the number of grid points becomes small, the effect of the temperature being fixed in the boundary layer (explained in Section 4.2) will introduce slightly hotter solutions near the boundaries. As one would expect, this makes little difference at finer resolution.

Fig. 7 presents a summary of these results. The upper (lower) panel shows a log-linear (linear–linear) plot of the temperature at various locations in the grid as a function of the number of grid points, which are increased (by factors of 2) from 32 up to 2048. In each case, *Lare* is started from the same initial uniform temperature and allowed to relaxed to the equilibrium. Once relaxed, the four chosen locations are the null point (black), (0.25, 0.25) (green), (0.5, 0.5) (blue) and (0.75, 0.75) (red). Note that, for each point *apart* for the null point, the temperatures converge rapidly, with increased number of grid points when $B^2_{\rm min} = 10^{-10}$. However, at the null point, the temperature continues to increase, despite the increase in the number of grid points used. In the upper panel,

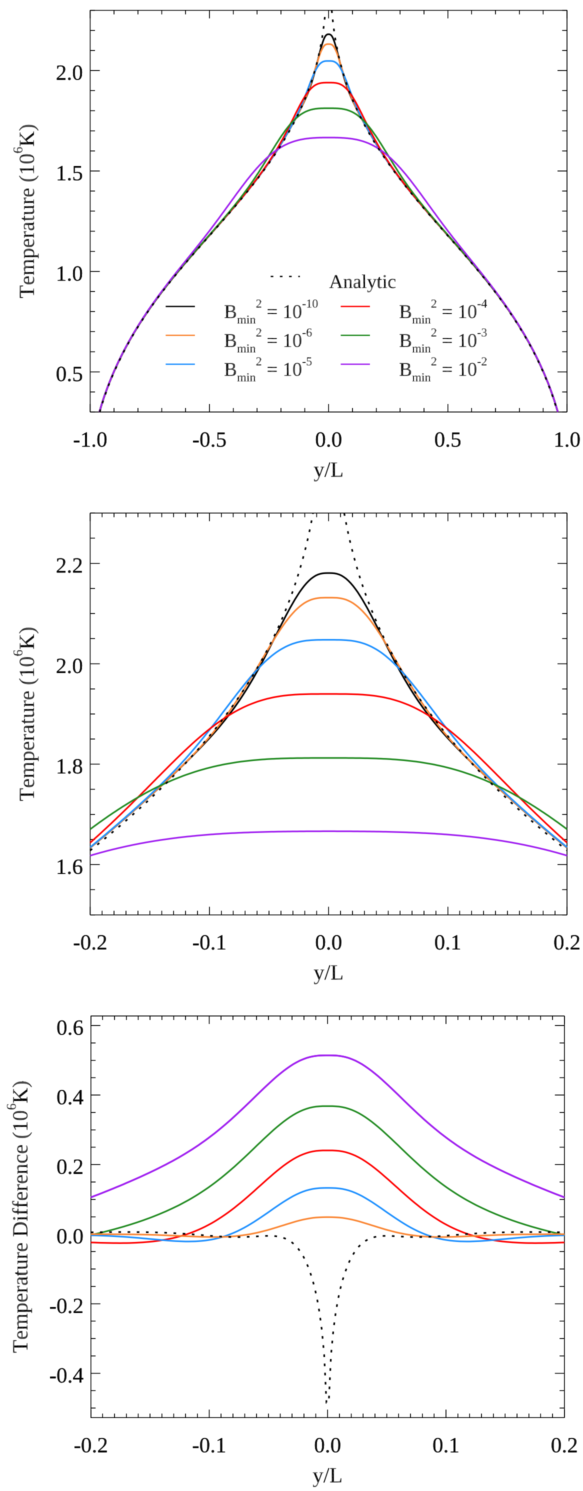

Figure 5. The upper two panels show the temperature along $y = z$. Each curve represents a specific value for $\mathrm{B}^2_{\mathrm{min}}$, which is stated in the legend of the top panel. The top panel shows the full range in y/L and the middle figure shows an expanded range in y/L. The bottom panel shows each of the solutions subtracted from the $\mathrm{B}^2_{\mathrm{min}} = 10^{-10}$ solution.

the null temperature appears to continue to grow linearly, when plotted as a function of the logarithm of the number of grid points and there is no evidence of convergence at the null. These results, based on the default value of B^2_{min}, demonstrate clearly that the temperature at the null point *cannot* be trusted as there is no evidence of convergence.

The black dotted curve in the upper panel of Fig. 7 signifies the same measurement as the black solid curve, but for a set of simulations where $B^2_{\mathrm{min}} = 10^{-4}$. In this case, the temperature at the null converges at 128 cells per dimension. This highlights that *Lare* is capable of resolving the problem (at typical resolutions) if we use an enhanced value for B_{min}, in a manner similar to the numerical treatment of electrical resistivity. This keeps the perpendicular conductivity physically relevant and not due to numerical effects.

Using the analytic solution in equation (29), we can evaluate the temperature at the cell centre nearest to the null point. This is at $y = \delta y/2$, $z = \delta z/2$. Remember that temperature is evaluated at cell centre and the null point is at a cell corner. Thus, setting $\delta y = \delta z = h$, the solution gives, to leading order in h,

$$\bar{G} \approx \bar{G}_b - \frac{1}{4} - \frac{1}{2}\ln|h| \; . \tag{33}$$

Thus, we expect the temperature at the null to increase with the logarithm of the number of grid points, as indicated in the upper figure in Fig. 7. Equation (33) does not include numerical diffusion and provides an upper bound on the null temperature. This emphasises the importance of numerically checking whether results are robust or not. If the physical variables do not change, when increasing the number of gridpoints (improved resolution), then the results are numerically converged.

5 DISCUSSION AND CONCLUSIONS

In this paper, we investigated the thermodynamic response of a coronal magnetic null point subject to two forms of steady heating: spatially uniform and proportional to B^2. For the case of uniform heating (assuming thermal conduction is field-aligned) we find singular analytical solutions for the equilibrium temperature, at the null and along the separatrices. This is because the vanishing magnetic field at the null has an infinite area factor, $\mathcal{A}(s)$, meaning field-aligned conduction is entirely inhibited there and cannot balance any heating. The solution becomes finite when one accounts for the enhancement of cross-field thermal conduction as the magnetic field weakens. Under coronal conditions, the extent of the weak-field region is confined very close to the null. Within this region, thermal conduction is largely isotropic and balances heating at the null. However, due to the small size of the weak-field region, the range of the cross-field conduction is short and so the null and separatrices remain significantly hotter than their surroundings. Conversely, when heating is proportional to B^2, the temperature is uniform about the null and there are no singular solutions, with or without cross-field thermal conduction.

The contrasting solutions due to the two forms of heating highlight the importance of understanding how nulls are heated. Specifically, if there is heating at a null (as in the uniform heating case) it may be much hotter than its surroundings and hence observable (e.g. Cheng et al. 2023). However, Mason, Antiochos & Viall (2019) suggests that coronal rain can form ubiquitously in some null topologies, if the heating is primarily at the footpoints of loops (as approximated by the B^2 heating case). Coronal rain formation relies on radiative losses

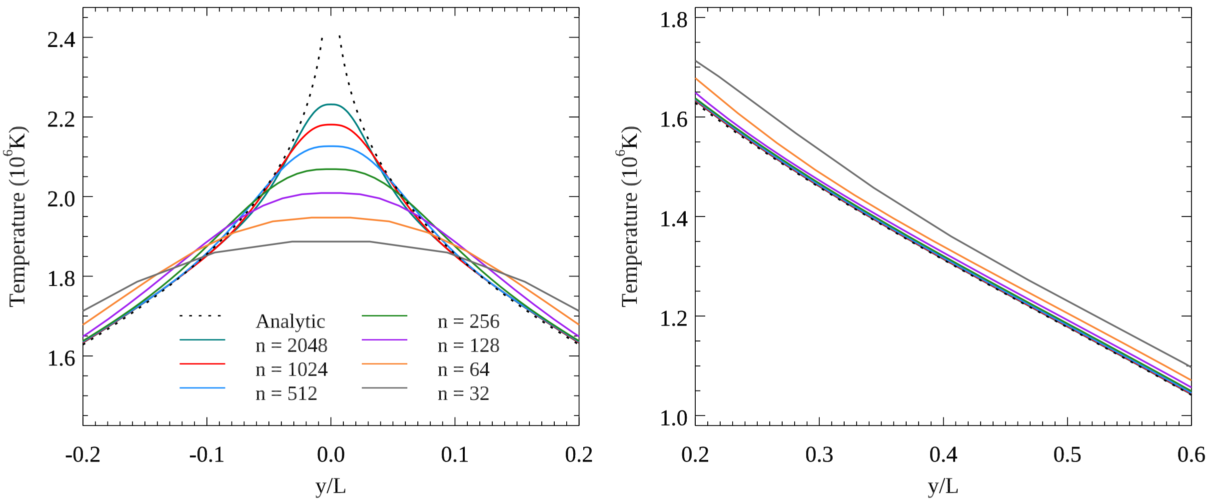

Figure 6. Temperature along $y = z$ for the analytic solution and the various resolution simulations of uniform heating, for $|y/L| < 0.2$ (left) and $0.2 < y/L < 0.6$ (right). The legend in left plot describes each curve.

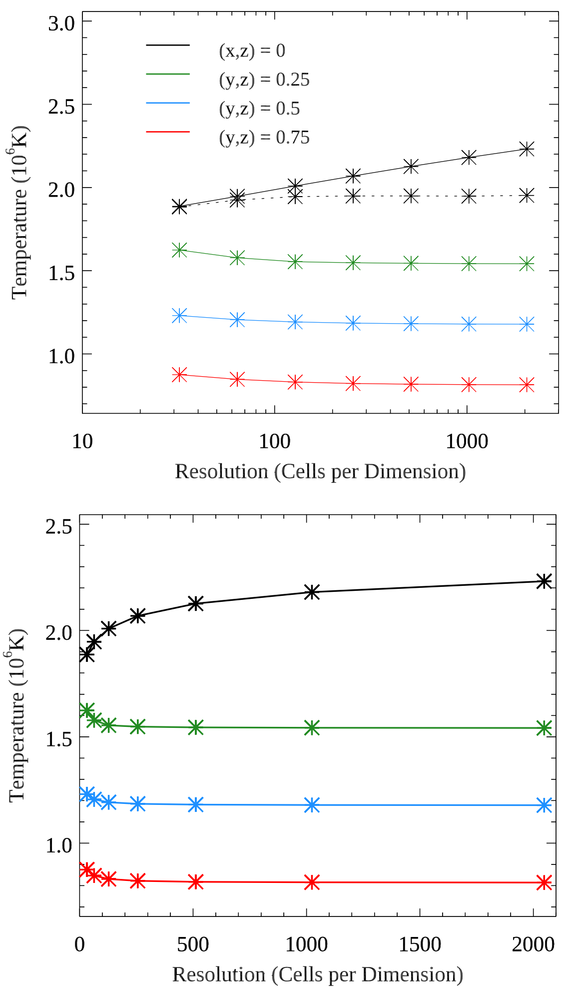

Figure 7. Temperature at various points versus simulation resolution, the legend in the upper plot describes each curve. Upper plot uses a log-linear scale and the lower linear–linear. All solid curves use $B_{\rm min}^2 = 10^{-10}$ and the dotted curve in the upper plot uses $B_{\rm min}^2 = 10^{-4}$.

and hence is not present in this investigation, but will be considered in future works.

Exactly how a null is heated remains unclear, as there are numerous mechanisms that may be responsible. These may, or may not, heat the null itself and can differ from the simple forms of heating investigated in this work. MHD waves can propagate energy and heat the vicinity of a null point. McLaughlin & Hood (2004) find that Alfvén waves, that are incident on a null point, tend to accumulate along the separatrices, forming currents that may cause heating. Conversely, fast modes are refracted by null point magnetic fields, focusing wave energy towards the null (e.g. McLaughlin & Hood 2005; McLaughlin et al. 2009, 2019). Our investigation suggests that if this energy is dissipated as heating at the null, the null point and separatrices ought to be hotter than their surroundings. In this case, the equilibrium solution would strongly depend on the nature of thermal conduction at the null point, which this work shows must be treated properly.

Heating may also occur near, but not at, a null point or its separatrices. Prokopyszyn et al. (2019) finds that Alfvén waves excited on line-tied fields near a null can resonate, forming strong currents that contribute to Ohmic heating. Additionally, the line-tied fields support Alfvén wave phase mixing (e.g. Heyvaerts & Priest 1983), adding to the heating near the null. Arbitrary wave disturbances can displace separatrices causing a null point to collapse, introducing a current sheet (and Ohmic heating) around the null. Currently, there is no general consensus of how Ohmic heating will manifest itself about a null, understanding this is the purpose of this and future works.

A final point to mention, is that this paper provides a model problem for different MHD codes to test how well they deal with magnetic null points. Specifically, it provides a problem to test whether numerical results have converged in the sense they are not dependent on the grid resolution. To achieve a resolved solution at a null, one must resolve cross-field thermal conduction even if it requires enhancing the cross-field conductivity, by increasing $B_{\rm min}$. The advantage of using $B_{\rm min}$, rather than relying on numerical diffusion, to limit the temperature near the null, is that real physical processes are involved. They may be enhanced but they treat the flow of heat in a physically correct manner.

We have focused on *coronal* null points (meaning $B_{\rm min}$ should be very small) because they allow us to neglect optically thin radiation, (as a reasonable approximation) permitting analytical solutions. Note though that for cooler plasmas, $B_{\rm min}$ can be much larger. Additionally, optically thin radiation is important in the transition region. These effects may introduce interesting consequences for cooling, and steady state temperatures, at null points in transition region plasmas and will be investigated in future projects.

ACKNOWLEDGEMENTS

DJ, AWH, and JR gratefully acknowledge the financial support of the Science and Technology Facilities Council (STFC) through Consolidated Grants ST/S000402/1 and ST/W001195/1 to the University of St Andrews. CDJ acknowledges support from the NASA GSFC Heliophysics Internal Scientist Funding Model competitive work package program (PI Jim Klimchuk).

DATA AVAILABILITY

The Lare3D code, used to produce the simulations in this work, is freely available and may be found at https://github.com/Warwick-Plasma/Lare3d and is described in Arber et al. (2001).

REFERENCES

Aitken A. C., 1927, Proc. Roy. Soc. Edinburgh, 46, 289
Antiochos S. K., Klimchuk J. A., 1991, ApJ, 378, 372
Antiochos S. K., Sturrock P. A., 1976, Sol. Phys., 49, 359
Arber T. D., Longbottom A. W., Gerrard C. L., Milne A. M., 2001, J. Comput. Phys., 171, 151
Balescu R., 1988a, Transport Processes in Plasmas, Classical Transport Theory. North-Holland, Netherlands
Balescu R., 1988b, Transport Processes in Plasmas: Neoclassical transport theory, Transport Processes in Plasmas. North-Holland, Netherlands
Barnes W. T., Cargill P. J., Bradshaw S. J., 2016, ApJ, 829, 31
Botha G. J., Arber T. D., Nakariakov V. M., Keenan F. P., 2000, A&A, 363, 1186
Boyd T. J. M., Sanderson J. J., 2003, The Physics of Plasmas. Cambridge Univ. Press, Cambridge,
Braginskii S. I., 1965, Rev. Plasma Phys., 1, 205
Brown D. S., Priest E. R., 2001, A&A, 367, 339
Bulanov S., Syrovatskii S., 1980, Sov. J. Plasma Phys. (Engl. Transl.), 6, 661
Caramana E., Shashkov M., Whalen P., 1998, J. Comput. Phys., 144, 70
Cargill P. J., 1993, Sol. Phys., 147, 263
Cargill P. J., Bradshaw S. J., Klimchuk J. A., Barnes W. T., 2022, MNRAS, 509, 4420
Cargill P. J., Mariska J. T., Antiochos S. K., 1995, ApJ, 439, 1034
Cargill P. J., Warren H. P., Bradshaw S. J., 2015, Philos. T. R. Soc. A: Math. Phys. Eng. Sci., 373, 20140260
Cheng X. et al., 2023, Nat. Commun., 14, 2107
Close R. M., Parnell C. E., Priest E. R., 2004, Sol. Phys., 225, 21
Craig I. J. D., McClymont A. N., 1991, ApJ, 371, L41
De Moortel I., Browning P., 2015, Philos. T. R. Soc. A: Math. Phys. Eng. Sci., 373, 20140269
Evans C. R., Hawley J. F., 1988, ApJ, 332, 659.
Froment C., Auchère F., Mikić Z., Aulanier G., Bocchialini K., Buchlin E., Solomon J., Soubrié E., 2018, ApJ, 855, 52
Galsgaard K., Pontin D. I., 2011, A&A, 534, A2
Gerrard C. L., Arber T. D., Hood A. W., Van der Linden R. A. M., 2001, A&A, 373, 1089
Gerrard C. L., Brown D. S., Mellor C., Arber T. D., Hood A. W., 2003, Sol. Phys., 213, 39
Heyvaerts J., Priest E. R., 1983, A&A, 117, 220
Hood A. W., Browning P. K., Van der Linden R. A. M., 2009, A&A, 506, 913
Klimchuk J. A., 2006, Sol. Phys., 234, 41
Lau Y.-T., Finn J. M., 1990, ApJ, 350, 672
Longcope D. W., Parnell C. E., 2009, Sol. Phys., 254, 51
Mason E. I., Antiochos S. K., Viall N. M., 2019, ApJ, 874, L33
McLaughlin J. A., 2013, JA&A, 34, 223
McLaughlin J. A., De Moortel I., Hood A. W., Brady C. S., 2009, A&A, 493, 227
McLaughlin J. A., Hood A. W., 2004, A&A, 420, 1129
McLaughlin J. A., Hood A. W., 2005, A&A, 435, 313
McLaughlin J. A., Hood A. W., 2006, A&A, 459, 641
McLaughlin J. A., Hood A. W., De Moortel I., 2011, SSR, 158, 205
McLaughlin J. A., Thurgood J. O., Botha G. J. J., Wiggs J. A., 2019, MNRAS, 484, 1390
Parenti S., Zanna G. d., Petralia A., Reale F., Teriaca L., Testa P., Mason H. E., 2017, ApJ, 846, 25
Parker E. N., 1972, ApJ, 174, 499
Parker E. N., 1988, ApJ, 330, 474
Parnell C. E., De Moortel I., 2012, Philos. T. R. Soc. A: Math. Phys. Eng. Sci., 370, 3217
Parnell C. E., Smith J. M., Neukirch T., Priest E. R., 1996, Physics of Plasmas, 3, 759
Pontin D. I., Candelaresi S., Russell A. J. B., Hornig G., 2016, Plasma Phys. Control. Fusion, 58, 54008
Prokopyszyn A. P. K., Hood A. W., De Moortel I., 2019, A&A, 624, A90
Reale F., Testa P., Klimchuk J. A., Susanna P., 2009, ApJ, 698, 756
Régnier S., Parnell C. E., Haynes A. L., 2008, A&A, 484, L47
Reid J., Cargill P. J., Hood A. W., Parnell C. E., Arber T. D., 2020, A&A, 633, A158
Rosner R., Tucker W. H., Vaiana G. S., 1978, ApJ, 220, 643
Testa P., Reale F., 2012, ApJ, 750, L10
Van Doorsselaere T., Andries J., Poedts S., 2007, A&A, 471, 311
Van Leer B., 1997, J. Comput. Phys., 135, 229
Woods L. C., 1987, Principles of Magnetoplasma Dynamics, Oxford science publications, Clarendon Press, Oxford
Zirker J. B., Cleveland F. M., 1993, Sol. Phys., 144, 341

APPENDIX A: THE FORM OF THERMAL CONDUCTION

Braginskii (1965) presents an approximation for the thermal conductivity tensor. The approximation is derived using the Chapman–Enskog method, with an infinite series of Laguerre–Sonine polynomials and using spherical harmonics. Balescu (1988a), by contrast, uses irreducible tensorial Hermite polynomials, in a Cartesian representation, and he overcomes the slow convergence of the Braginskii approach (see also Boyd & Sanderson 2003). There are three components of the conductivity tensor representing thermal conduction due to the temperature gradient parallel to the magnetic field, $\kappa_\parallel$, temperature gradient perpendicular to the magnetic field, $\kappa_\perp$ and in the third orthogonal direction, $\kappa_\wedge$. Since, in this 2D problem the third direction is an ignorable coordinate, there is no variation in the third direction and the effect of $\kappa_\wedge$ does not contribute to thermal conduction. Normally, we would expect that parallel conductivity provides an adequate contribution to thermal conduction, as the perpendicular conductivity is only important at the null point and is negligible away from it. Also note that the forms for $\kappa_\parallel$, $\kappa_\perp$ and $\kappa_\wedge$ are derived for classical transport theory in a straight field and may differ for anomalous transport theory in a curved field. Any additional effects due to field line curvature are not discussed here. However, the fact remains that $\kappa_\perp \to \kappa_\parallel$ and $\kappa_\wedge \to 0$, as $B \to 0$.

Balescu (1988a) derives the parallel thermal conductivity component, $\kappa_\parallel$, parallel to the magnetic field, and expresses the perpendicular conductivity component, $\kappa_\perp$ perpendicular to the magnetic field as a function of $\omega\tau$, where $\omega = eB/m_e$ is the electron gyrofrequency, with e the electron charge, B the magnetic field strength and m_e the electron mass, and τ is the electron collision time. τ is defined by equation (9) as

$$\tau = \left(\frac{\sqrt{4\pi\varepsilon_0}}{e}\right)^4 \frac{3\sqrt{m_e}(k_B T)^{3/2}}{4\sqrt{2\pi}n\lambda}.$$

Balescu (1988a) obtains different approximations to $\kappa_\perp$ by using more moments in its derivation from the plasma distribution function. In all cases,

$$\kappa_\perp = \frac{F(\omega\tau)}{G(\omega\tau)}\kappa_\parallel \ , \tag{A1}$$

where F and G are polynomials in $\omega\tau$ of the form

$$F(\omega\tau) = F_{n,0} + F_{n,1}(\omega\tau)^2 + \cdots F_{n,n}(\omega\tau)^{2n} \ , \tag{A2}$$

and

$$G(\omega\tau) = G_{n,0} + G_{n,1}(\omega\tau)^2 + \cdots G_{n,n+1}(\omega\tau)^{2n+2} \ . \tag{A3}$$

The constants, $F_{n,i}$ and $G_{n,i}$ depend on the value of n, namely the highest power in the truncation of the series. The series do seem to converge quickly. However, in our case we are only interested in ensuring that the numerical code does *not* end up with a division by zero at a coronal null point and so we take the simplest approximation, namely $n = 0$ and $F_{0,0} = G_{0,0} = G_{0,1} = 1$. This gives the correct form for $\kappa_\perp$ for strong magnetic fields, where $\omega\tau \gg 1$, and correctly reduces to $\kappa_\parallel$ where the magnetic field vanishes or is small.

This paper has been typeset from a TEX/LATEX file prepared by the author.